NUMERICAL SOLUTION OF 2-D SLAMMING PROBLEM WITH A CIP METHOD

QINGYONG YANG

Numerical Solution of 2-D Slamming Problem with a CIP Method

by

©Qingyong Yang
St. John's, Newfoundland, Canada

B.Eng., Dalian University of Technology, China (2003)
M.Eng., Dalian University of Technology, China (2005)

A thesis submitted to the
School of Graduate Studies
in partial fulfillment of the
requirements for the degree of
Master of Engineering

Faculty of Engineering and Applied Science
Memorial University of Newfoundland

December 2007

Abstract

This thesis presents numerical solutions of the slamming problem for 2-D sections entering calm water. The highly nonlinear water entry problem governed by the Navier-Stokes equations was solved by a Constrained Interpolation Profile (CIP)-based finite difference method on a fixed Cartesian grid. In the computation, the CIP method was employed for the advection calculations and a pressured-based algorithm was applied for non-advection calculations. The free surfaces and the body boundaries were captured using color functions. For the pressure calculation, a Poisson-type equation was solved at each time step by the Conjugate Gradient (CG) iterative method.

Validation studies have been carried out for wedges with various deadrise angles and for a bow flare section. Pressures, free surface elevations and hydrodynamic forces were compared with experimental results and numerical solutions by the boundary element method (BEM), the volume of fluid (VOF) method, and the smoothed particle hydrodynamics (SPH) method.

Acknowledgements

I would like to give my foremost appreciation and thanks to my supervisor, Dr. Wei Qiu, who greatly enhanced my interest in Marine Hydrodynamics, for his continuous academic guidance with patience, kindness, encouragement, and support throughout this thesis work. His advice and guidance have been invaluable to the development of this work.

I also wish to express my deep appreciation to the Canadian Foundation for Innovation (CFI) and the Natural Sciences and Engineering Research Council (NSERC) of Canada. This work would not have been completed without their financial support.

Many thanks are extended to my colleagues and friends at the Advanced Marine Hydrodynamics Laboratory, Hui Yin, Lei Liu, Min Zhang and Chao Guo, for the useful discussions and suggestions at various stages of the work. I also would like to acknowledge the advice from Dr. S. Ni.

Finally, I would like to give my special thanks to my parents, X.L. Wang and E.Z. Yang. I am profoundly grateful for their love, support and understanding.

Contents

List of Figures

Nomenclature

$\mathbf{A}$	square matrix
B	breadth of the wedge
$\mathbf{b}$	column vector
c_s	sound speed
f_i	body force
F_i	hydrodynamic force
F_i^P	hydrodynamic force due to pressure
F_i^V	hydrodynamic force due to friction
n_k	kth component of the outward unit normal vector
p	pressure
T	temperature
t	time
u_i	velocity component
x_i	Cartesian coordinate
δ	Kronecker's delta function

$\triangle t$	time step
$\triangle x$	grid spacing in ox direction
$\triangle y$	grid spacing in oy direction
ϵ	small positive constant
μ	dynamic viscosity coefficient
ρ	mass density
σ	total stress
ϕ_m	density function
Ω	computational domain

Chapter 1

Introduction

1.1 Background and Motivation

When a ship travels in heavy seas, large-amplitude ship motion can result in bow-flare water impact. It will subsequently cause severe damages to ship structures. Bow-flare slamming occurs for high relative speed of the bow-flare to the water surface, and the duration of impact takes a very short time, usually lasting for less than a second. Jets run up on both sides of the bow and move away from it. The maximum slamming pressure occurs near the spray roots on the ship hull before the flow separates, which is much larger than other wave loads. Therefore, it is essential to predict the pressure distribution induced by the bow-flare water impact in the ship design.

The prediction of slamming force can be achieved by solving the Laplace equation with nonlinear free-surface boundary conditions or by solving the Navier-Stokes equations. In the numerical simulation, the bow-flare water impact problem is commonly simplified as an entry of a two-dimensional wedge into calm water, see Figure 1-1, and it is assumed that the velocity of the wedge entering calm water is equal to the relative velocity of the wedge and the moving free surface. The major difficulty in solving the slamming problem arises from their extremely complicated

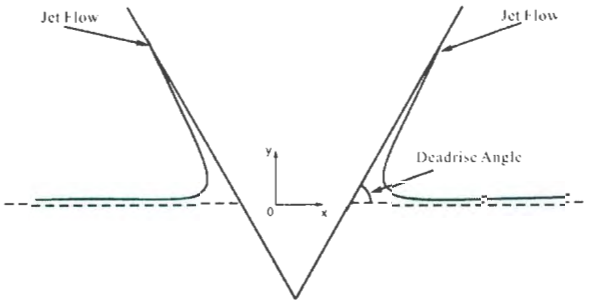

Figure 1-1: Two-dimensional entry of a wedge into calm water

hydrodynamic phenomena where the compressibility of water, air cushions, air bubbles, and hydro-elasticity may be revelent. It is necessary to deal with the highly distorted or breaking free surfaces, and to treat large gradient of physical quantities at interfaces in the multiphase computational domain.

This thesis presents a numerical method based on solving the Navier-Stokes equations to predict the slamming loads on 2-D sections.

1.2 Literature Review

The water-entry problem of a wedge has been extensively studied by many researchers. The theoretical analysis of the similarity flow induced by the wedge entry was first conducted by Wagner (1932). Armand and Cointe (1986), Cointe (1991) and Howison *et al.* (1991) extended Wagner's theory to analyze the wedge entry problem using matched asymptotic expansions for wedges with small deadrise. Furthermore, Dobrovol'skaya (1969) developed an analytical solution in terms of a nonlinear singular integral equation for the problem of the symmetrical entry of a wedge into calm water. Based on the work of Vinje and Brevig (1981), Greenhow (1987) used Cauchy's formula to solve the wedge entry problem. In his work, both gravity and nonlinear free surface conditions were taken into account. Zhao and Faltinsen (1993) studied the water entry of a wedge using boundary element method with constant elements. The jet tip at the intersection point of the body surface and

the free surface was cut and two small constant elements were distributed. There are numerical difficulties to trace the water particles in the intersection point. Lin *et al.* (1984) presented an approach to treat the difficulties. In their work, the boundary integral equation derived from Cauchy's formula was discretized using linear elements so that the intersection points can be used as the collocation points. Chuang *et al.* (2006) developed a boundary element method based on desingularized Cauchy's formula. A numerical approach was also developed to remove the corner singularity at the intersection point of body surface and free surface.

Although great progress has been made in solving the water-entry problem with potential-flow based methods, there are difficulties for these methods to treat highly distorted or breaking free surface. These difficulties can be overcome by the computational fluid dynamics (CFD) methods based on solving the Navier-Stokes equations. One of the CFD methods is the volume of fluid (VOF) method. In the VOF method, a VOF function, F, is introduced with values between zero and one, indicating the fractional volume of a cell that is filled with a certain fluid. The piecewise constant reconstruction are commonly used to reconstruct the VOF function. Kleefsman *et al.* (2005) have solved the 2-D slamming problem of symmetric bodies by the VOF method, and the finite volume discretization with a cut-cell method were applied on a fixed Cartesian grid.

Another method that is used in the slamming computations is the smoothed particle hydrodynamics (SPH) method, which is a meshless method. Particles are distributied in the flow and every particle carries mass and velocity. A particle is influenced by other particles that are within a certain distance from the particle. The method can handle the large deformation of the fluid interface. Kim *et al.* (2007) used the SPH method to simulate the water entry of asymmetric bodies. A large number of particles are distributed in the computational domain and the ghost particle approach was used to treat the solid boundary.

In this thesis, a constrained interpolation profile (CIP) method which was

proposed by Xiao (1999) and further developed by Hu and Kashiwagi (2004) for violent free surface flow, is applied to solve the 2-D water entry problem. The CIP method is based on a high-order upwind scheme and solves the advection terms in the Navier-Stokes equations. Sub-cell resolution is obtained by using both the advection function and its spatial derivatives at the grid points to estimate the function inside the cell. The CIP method as an interface capturing method does not need an adaptive grid system and therefore removes the problems of grid distortion caused by interface breakup and topology change. The material surface can be captured by almost one grid throughout the computation (Yabe *et al.*, 2001). Furthermore, the scheme can treat multiple phases (Yabe *et al.*, 2000). A pressure-based algorithm coupled with CIP, namely CIP combined and unified procedure (CCUP), has been proved to be stable and robust in solving the slamming problem (Hu and Kashiwagi, 2004). Zhu *et al.* (2005) studied the water entry and the exit of a horizontal circular cylinder using a finite-difference method based on the CIP algorithm.

1.3 Thesis Contents

In this work, the CIP-based finite difference method is employed to compute symmetric and asymmetric water entry of wedges with various deadrise angles and the water entry of a bow flare section.

This thesis is organized as follows. Chapter 2 introduces the governing equations and boundary conditions for the two-dimensional water-entry problem. The CIP method is explained. The fractional step approach and the pressure-based method are briefly described. The interface capturing scheme, the calculation for hydrodynamic forces acting on a moving solid body, and the computational procedure are outlined. In Chapter 3, numerical results of 2-D water entry problems are presented. Computations were first carried out for symmetric water entry of wedges with deadrise angle of 30^o, 40^o and 60^o. The pressure distributions, free surface elevations and

hydrodynamic forces are presented. The free surface elevations of a wedge with deadrise angle of 45^o during asymmetric drop (tilt angle of 20^o) were also computed. Numerical results were compared with experimental results and solutions by the BEM, the VOF method and the SPH method. The water entry of a bow flare section was also computed. Conclusions are given in Chapter 4.

Chapter 2

Mathematical Formulation

2.1 Governing Equation

The flow under consideration is assumed to be a two-dimensional flow. The differential equations governing the compressible and viscous fluid are given:

$$\frac{\partial \rho}{\partial t} + u_i \frac{\partial \rho}{\partial x_i} = -\rho \frac{\partial u_i}{\partial x_i} \tag{2.1}$$

$$\frac{\partial u_i}{\partial t} + u_j \frac{\partial u_i}{\partial x_j} = -\frac{1}{\rho} \frac{\partial \sigma_{ij}}{\partial x_j} + f_i \tag{2.2}$$

where t is the time; x_i $(i = 1, 2)$ are the coordinates in a Cartesian coordinate system; ρ is the mass density; u_i are the velocity components; f_i are due to the gravity force.

As there is no temperature variation, the equation of state (EOS) for the 2-D water-entry problem is written as $p = f(\rho)$. Applying the EOS to Eq. 2.1, the pressure equation can be obtained as

$$\frac{\partial p}{\partial t} + u_i \frac{\partial p}{\partial x_i} = -\rho c_s^2 \frac{\partial u_i}{\partial x_i} \tag{2.3}$$

where, $c_s = \sqrt{\partial p / \partial \rho}$ is the sound speed, and p is the pressure.

For a Newtonian fluid, the total stress can be written as

$$\sigma_{ij} = -p\delta_{i,j} + 2\mu S_{ij} - 2\mu\delta_{i,j}S_{kk}/3$$

$$S_{i,j} = \frac{1}{2}(\frac{\partial u_i}{\partial x_j} + \frac{\partial u_j}{\partial x_i})$$

where, μ is the dynamic viscosity coefficient and δ_{ij} is the Kronecker's delta function.

2.2 Fractional Step Approach

By applying the fractional step approach, the numerical solution of governing equations, Eqs. 2.1 to 2.3, can be solved in three steps as follows.

1. Advection phase

$$\frac{\partial \rho}{\partial t} + u_i\frac{\partial \rho}{\partial x_i} = 0 \tag{2.4}$$

$$\frac{\partial u_i}{\partial t} + u_j\frac{\partial u_i}{\partial x_j} = 0 \tag{2.5}$$

$$\frac{\partial p}{\partial t} + u_i\frac{\partial p}{\partial x_i} = 0 \tag{2.6}$$

2. Non-advection phase I

$$\frac{\partial u_i}{\partial t} = \frac{2\mu}{\rho}\frac{\partial}{\partial x_j}(S_{ij} - \frac{1}{3}\delta_{ij}S_{kk}) + f_i \tag{2.7}$$

3. Non-advection phase II

$$\frac{\partial \rho}{\partial t} = -\rho\frac{\partial u_i}{\partial x_i} \tag{2.8}$$

$$\frac{\partial u_i}{\partial t} = -\frac{1}{\rho}\frac{\partial p}{\partial x_i} \tag{2.9}$$

$$\frac{\partial p}{\partial t} = -\rho c_s^2\frac{\partial u_i}{\partial x_i} \tag{2.10}$$

The fractional steps in the present numerical method are arranged in the order of advection phase, non-advection phase I, and non-advection phase II. The advection

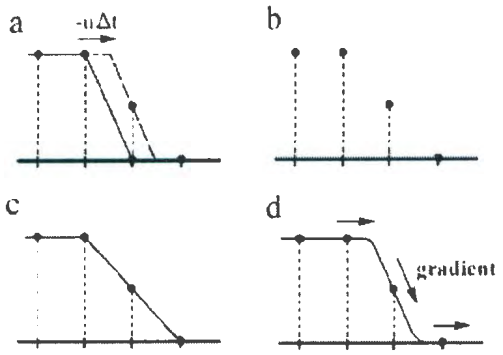

Figure 2-1: The principle of the CIP method

phase was computed by the CIP method. The non-advection I phase, which includes a viscous term and a source term, was solved by the central finite difference method. For the non-advection phase II, a pressure-based algorithm was employed.

2.3 CIP Method

2.3.1 The Principle of the CIP Method

The CIP method scheme can be treated as a kind of semi-Lagrangian method, which traces back along the characteristics in time. An interpolation of the initial profile is required to determine the value at the upstream departure points.

The strategy of the CIP method can be explained as follows by using an advection equation:

$$\frac{\partial f}{\partial t} + u\frac{\partial f}{\partial x} = 0 \tag{2.11}$$

When the velocity is constant, the solution of the equation gives a simple translation motion of waves with a velocity u. The initial profile (solid line of Fig. 2-1(a)) moves like a dashed line in a continuous representation. At this time,

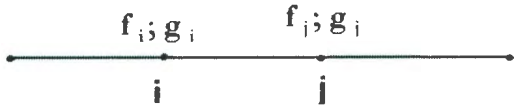

Figure 2-2: One-dimensional line element

the solution at grid points denoted by the filled circles is the same as the exact solution. However, if the dashed line are eliminated as shown in Fig. 2-1(b), then the information of the profile inside the grid cell is lost. Since it is difficult to imagine the original profile, it is natural to imagine a profile like that shown by the solid line in Fig. 2-1(c). Thus, numerical diffusion arises when we construct the profile by the linear interpolation. The reason why this solution becomes worse is that the behavior of the solution inside grid cell is neglected. The profile can be approximated as below.

Differentiating Eq. 2.11 with respect to the spatial variable x. we can obtain

$$\frac{\partial g}{\partial t} + u\frac{\partial g}{\partial x} = -\frac{\partial u}{\partial x}g \tag{2.12}$$

where, $g = \partial f/\partial x$ stands for the spatial derivative of f. In the simplest case where the velocity u is constant, Eq. 2.12 coincides with Eq. 2.11 and represents the propagation of spatial derivative with a velocity u. Using these equations, we can trace the time evolution of f and g. If g is predicted after propagation as shown by the arrows in Fig. 2-1(d), the profile after one step is limited to a specific profile. With this constraint of derivative (Eq. 2.12), the solution becomes much closer to the real solution. Most importantly, the solution can be kept consistent with Eq. 2.11 even inside the grid cell.

If two values of f and g are given at two grid points as in Fig. 2-2, the profile between these points can be interpolated by a cubic polynomial,

$$F(x) = ax^3 + bx^2 + cx + d$$

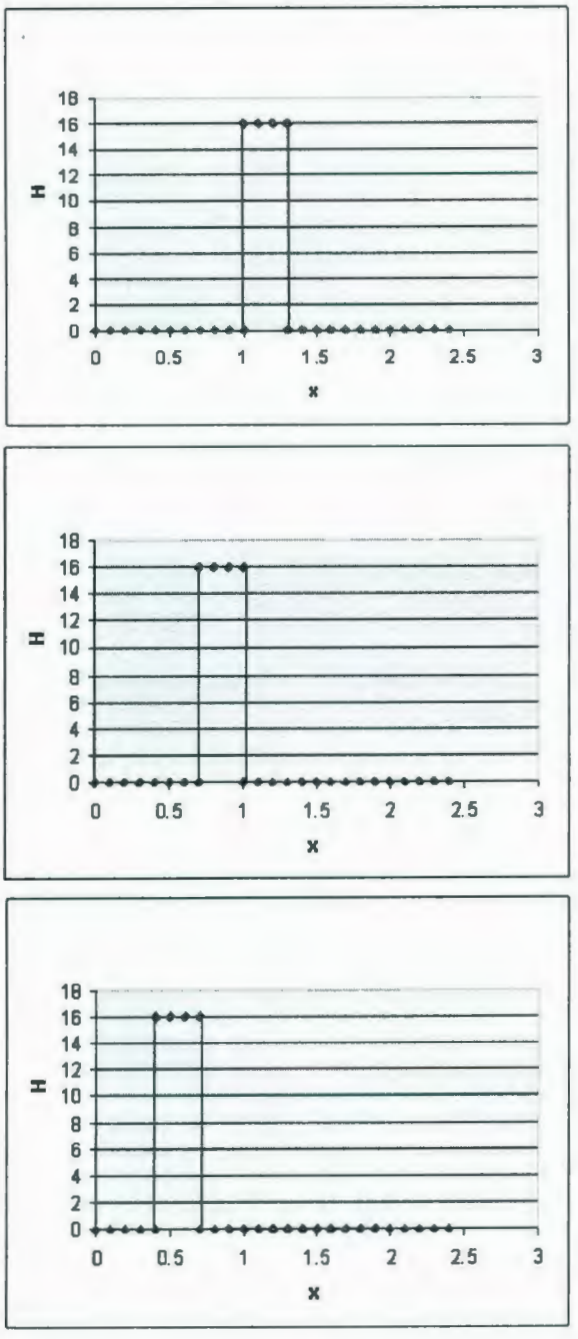

Figure 2-3: One-dimensional square wave propagation

The profile at the $n+1$ step can then be obtained by shifting the profile by $u\Delta t$, i.e.,

$$f^{n+1} = F(x - u\Delta t)$$

$$g^{n+1} = dF(x - u\Delta t)/dx$$

$$a_i = \frac{g_i + g_{iup}}{D^2} + \frac{2(f_i - f_{iup})}{D^3}$$

$$b_i = \frac{3(f_{iup} - f_i)}{D^2} - \frac{2g_i + g_{iup}}{D}$$

$$f_i^{n+1} = a_i\xi^3 + b_i\xi^2 + g_i^n\xi + f_i^n$$

$$g_i^{n+1} = 3a_i\xi^2 + 2b_i\xi + g_i^n$$

where, $\xi = -u\Delta t$, $D = -\Delta x$, $iup = i-1$ for $u > 0$; $\xi = u\Delta t$, $D = \Delta x$, $iup = i+1$ for $u < 0$. Fig. 2-3 shows the square wave propagation at several time instants with the CIP method. Note that only two points for constructing interpolation approximations are needed in one dimension. For calculating discontinuities or large gradients, a more compact scheme by which one can construct interpolation functions of high accuracy with fewer computational stencils is desirable. The CIP method seems to be attractive in this sense.

2.3.2 CIP Formulation in Two Dimensional Cases

In the CIP method, the first-order spatial derivatives of the interpolation function are treated as dependent variables. The governing equations for these derivatives in multi-dimensions are derived by differentiating the advection equation with respect to the spatial coordinates. With a special treatment of the first derivatives of the interpolation function, the CIP method achieves a compact form that uses only one mesh cell to construct the interpolation profile and provides subcell resolution.

One of the main efforts in semi-Lagrangian methods is constructing the

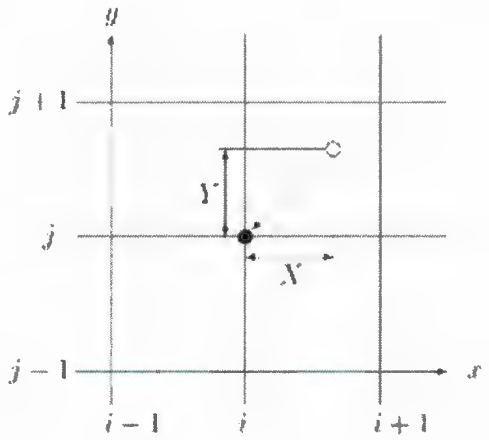

Figure 2-4: Model of spatial advection of χ in the case of $u < 0$ and $v < 0$

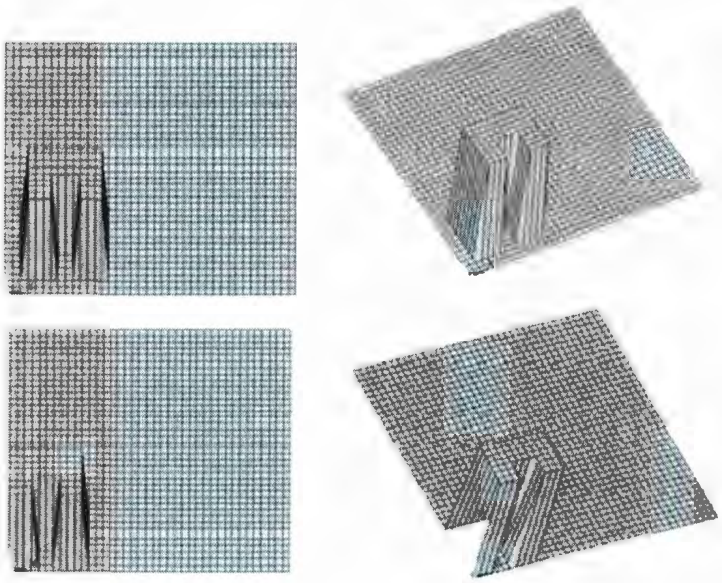

Figure 2-5: Two-dimensional profile propagation with the CIP

interpolation function based on grid values to determine the field value at a departure point not coinciding with a grid point. Several forms of the multi-dimensional cubic polynomial have been proposed. The simplest one proposed by Yabe *et al.* (2001) is given as

$$F(X,Y) = C_{30}X^3 + C_{21}X^2Y + C_{12}XY^2 + C_{03}Y^3$$

$$+C_{20}X^2 + C_{11}XY + C_{02}Y^2 + C_{10}X + C_{01}Y + C_{00}$$

$$F_x = 3C_{30}X^2 + 2C_{21}XY + C_{12}Y^2 + 2C_{20}X + C_{11}Y + C_{10}$$

$$F_y = C_{21}X^2 + 2C_{12}XY + 3C_{03}Y^2 + C_{11}X + 2C_{02}Y + C_{01}$$

where $X = x - x_i$ and $Y = y - y_i$ (see Fig. 2-4). There are ten unknown coefficients, C_{mn}, which will be determined as follows by the values of χ^n, χ^n_x, and χ^n_y at grid points (i,j), $(i+1,j)$, $(i,j+1)$, and the value of χ^n at the grid point $(i+1,j+1)$, where χ denotes objective values on grid points, e.g., ρ, p, u or v in the Navier-Stokes equations.

$$C_{00} = \chi^n(i,j)$$

$$C_{01} = \chi^n_y(i,j)$$

$$C_{10} = \chi^n_x(i,j)$$

$$C_{30} = [\xi(\chi^n_x(i+1,j) + \chi^n_x(i,j)) - 2(\chi^n(i+1,j) - \chi^n(i,j))]/\xi^3$$

$$C_{20} = [-\xi(\chi^n_x(i+1,j) + 2\chi^n_x(i,j)) + 3(\chi^n(i+1,j) - \chi^n(i,j))]/\xi^2$$

$$C_{03} = [\eta(\chi^n_y(i,j+1) + \chi^n_y(i,j)) - 2(\chi^n(i,j+1) - \chi^n(i,j))]/\eta^3$$

$$C_{02} = [-\eta(\chi^n_y(i,j+1) + 2\chi^n_y(i,j)) + 3(\chi^n(i,j+1) - \chi^n(i,j))]/\eta^2$$

$$C_{21} = [\chi^n_x(i+1,j+1) - \chi^n_x(i+1,j) - \chi^n_x(i,j+1) + \chi^n_x(i,j)]/(2\xi\eta)$$

$$C_{12} = [\chi^n_y(i+1,j+1) - \chi^n_y(i+1,j) - \chi^n_y(i,j+1) + \chi^n_y(i,j)]/(2\xi\eta)$$

$$C_{11} = [\chi^n(i+1,j+1) - \chi^n(i+1,j) - \chi^n(i,j+1) + \chi^n(i,j)]/(\xi\eta) - C_{21}\xi - C_{12}\eta$$

where $\xi = -\text{sign}(u) \triangle x$, $\eta = -\text{sign}(v) \triangle y$. Then the derivatives of F with respect to ξ and η, χ^*, χ^*_x, and χ^*_y can be obtained directly as follows:

$$\chi^*(i,j) = F(\xi', \eta')$$

$$\chi^*_x(i,j) = \frac{F(\xi,\eta)}{\partial\xi}|_{\xi=\xi',\eta=\eta'}$$

$$\chi^*_y(i,j) = \frac{F(\xi,\eta)}{\partial\eta}|_{\xi=\xi',\eta=\eta'}$$

with $\xi' = -u \triangle t$ and $\eta' = -v \triangle t$.

As shown in Fig. 2-5, the sharpness of the large gradients on corner points in the two-dimensional profile propagation could be maintained very well with the CIP method. The CIP method is adopted to capture the interfaces between different phases, such as the free surface and the solid boundary in this work.

2.3.3 The Computation of Spatial Derivatives

The CIP method was employed in the computation of the advection phase, where not only the objective value f, but also its spatial derivatives, f_x and f_y, have to be updated at every time step. Eqs. 2.4 to 2.6 can be written in a general form as

$$\frac{\partial f}{\partial t} + u\frac{\partial f}{\partial x} + v\frac{\partial f}{\partial y} = 0 \tag{2.13}$$

Differentiating it with respect to x gives

$$\frac{\partial^2 f}{\partial t \partial x} + \frac{\partial u}{\partial x}\frac{\partial f}{\partial x} + u\frac{\partial^2 f}{\partial x^2} + \frac{\partial v}{\partial x}\frac{\partial f}{\partial y} + v\frac{\partial^2 f}{\partial x \partial y} = 0 \tag{2.14}$$

Denoting $\frac{\partial f}{\partial x}$ as f_x and $\frac{\partial f}{\partial y}$ as f_y, the above equation can be rewritten as,

$$\frac{\partial f_x}{\partial t} + u\frac{\partial f_x}{\partial x} + v\frac{\partial f_x}{\partial y} = -(f_x\frac{\partial u}{\partial x} + f_y\frac{\partial v}{\partial x}) \tag{2.15}$$

The left hand side of this equation is a two-dimensional advection equation for f_x. The CIP method can be applied to solve it. The right hand side of this equation is a source term, and this can be calculated simply by the central differential scheme.

Similarly, Eqs. 2.4 to 2.6 can be partially differentiated with respect to y, and we can obtain

$$\frac{\partial f_y}{\partial t} + u\frac{\partial f_y}{\partial x} + v\frac{\partial f_y}{\partial y} = -(f_x\frac{\partial u}{\partial y} + f_y\frac{\partial v}{\partial y}). \tag{2.16}$$

2.4 Pressure-Based Algorithm

In an ordinary compressible fluid, the density ρ is solved from the mass conservation equation. After that, from the equation of state, schematically shown in Fig. 2-6 (Yabe *et al.*, 2001), the pressure can be calculated. At the low-density side, $p \propto \rho T$ for the ideal fluid and the dependence on ρT is relatively weak, but for solid or liquid density, p steeply rises as the density rises. This means that extremely high pressure is needed to compress solid or liquid. In other words, for solid or liquid, the sound speed, $c_s = (\partial p/\partial\rho)^{1/2}$, is very large. A small amount of density error, for example 10%, can lead to a large pressure pulse of 3-4 orders of magnitude.

Fortunately, if we rotate Fig. 2-6 by 90 degrees, the steep pressure curve becomes a flat density curve. It means that if we could first solve the pressure and then estimate the density, the problem at large density would be eliminated.

The pressure-based equation can be obtained as follows by taking the divergence of Eq. 2.9 and substituting $\partial u_i/\partial x_i$ into Eq. 2.10,

$$\frac{\partial}{\partial x_i}(\frac{1}{\rho^*}\frac{\partial p^{n+1}}{\partial x_i}) = \frac{p^{n+1} - p^*}{\rho^* c_s^2 \Delta t^2} + \frac{1}{\Delta t}\frac{\partial u_i^{**}}{\partial x_i} \tag{2.17}$$

where the superscripts $*$ and $**$ indicate the provisional values before and after the calculation of non-advection phase I. Eq. 2.17 shows that $(\nabla p/\rho)$ is continuous at sharp discontinuities. In this case, the density changes by several orders of magnitude

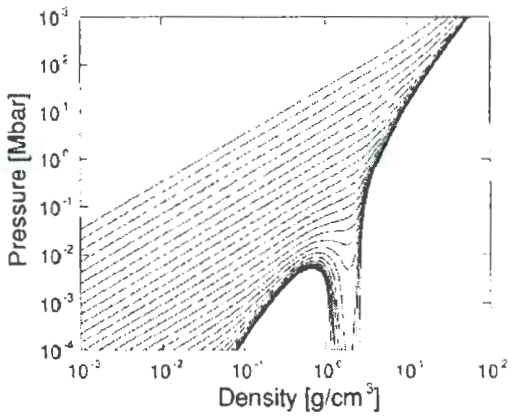

Figure 2-6: An example of an equation of state

at the boundary, for example, between liquid and gas, and the pressure gradient must be calculated accurately enough to ensure continuous change. The equation works robustly even with a density ratio larger than 1000 and the multiphase computations can be carried out.

For a perfect incompressible fluid, we can assume $c_s = \infty$, a simpler Poisson equation can be obtained as below:

$$\frac{\partial}{\partial x_i}(\frac{1}{\rho^*}\frac{\partial p^{n+1}}{\partial x_i}) = \frac{1}{\Delta t}\frac{\partial u_i^{**}}{\partial x_i} \tag{2.18}$$

This is a conventional Poisson equation for incompressible flows and it is valid for liquid, gas and solid phases. The solution of Eq. 2.18 provides the pressure distribution in the whole computation domain. The pressure distribution obtained inside the solid body is a fictitious one, which satisfies the divergence free condition of the velocity field (Hu and Kashiwagi, 2007). With this treatment, the boundary condition for pressure at the interface between different phases is not required.

In this work the finite difference method is applied to solve Eq. 2.18. The central difference formulas for the first order derivative on uniform grid are as follows:

$$(p_x)_{ij} \equiv (\frac{\partial p}{\partial x})_{ij} = \frac{p_{i+1,j} - p_{i-1,j}}{2\Delta x} \tag{2.19}$$

$$(p_y)_{ij} \equiv (\frac{\partial p}{\partial y})_{ij} = \frac{p_{i,j+1} - p_{i,j-1}}{2\Delta y} \tag{2.20}$$

The central difference formulas for the second derivatives are

$$(p_{xx})_{ij} \equiv (\frac{\partial^2 p}{\partial x^2})_{ij} = \frac{p_{i+1,j} - 2p_{i,j} + p_{i-1,j}}{\Delta x^2} \tag{2.21}$$

$$(p_{yy})_{ij} \equiv (\frac{\partial^2 p}{\partial y^2})_{ij} = \frac{p_{i,j+1} - 2p_{i,j} + p_{i.j-1}}{\Delta y^2} \tag{2.22}$$

Applying Eqs. 2.19 to 2.22, linear equations, $\mathbf{Ax} = \mathbf{b}$, can be obtained from Eq. 2.18, in which $\mathbf{x}$ is an unknown column vector of order n, $\mathbf{b}$ is a known vector of n components, and $\mathbf{A}$ is a known, square, symmetric, positive-definite matrix and given by the following square matrix:

$$\mathbf{A} = \begin{bmatrix} \alpha & \beta & 0 & \gamma & 0 & 0 & 0 & 0 & 0 \\ \beta & \alpha & \beta & 0 & \gamma & 0 & 0 & 0 & 0 \\ 0 & \beta & \alpha & \beta & 0 & \gamma & 0 & 0 & 0 \\ \gamma & 0 & \beta & \alpha & \beta & 0 & \gamma & 0 & 0 \\ 0 & \gamma & 0 & \beta & \alpha & \beta & 0 & \gamma & 0 \\ 0 & 0 & \gamma & 0 & \beta & \alpha & \beta & 0 & \gamma \\ 0 & 0 & 0 & \gamma & 0 & \beta & \alpha & \beta & 0 \\ 0 & 0 & 0 & 0 & \gamma & 0 & \beta & \alpha & \beta \\ 0 & 0 & 0 & 0 & 0 & \gamma & 0 & \beta & \alpha \end{bmatrix}$$

where α, β and γ are known constant coefficients. On a uniform grid, $\alpha = -\frac{2}{\rho^*}(\frac{1}{\Delta x^2} + \frac{1}{\Delta y^2})$, $\beta = \frac{1}{\rho^*}(\frac{1}{\Delta x^2})$, and $\gamma = \frac{1}{\rho^*}(\frac{1}{\Delta y^2})$, where Δx and Δy are the grid spacings in the x and y directions, respectively. The linear equations can be solved by the conjugate

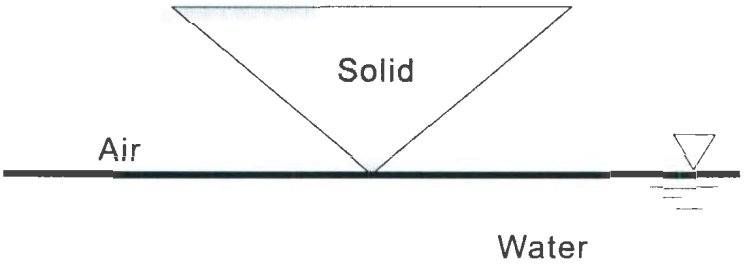

Figure 2-7: Schematic view of a numerical simulation for water entry.

gradient iterative method.

Furthermore, the matrix **A** is symmetric on a uniform grid. The half band width form can be used to reduce the storage. For the non-uniform grids, **A** is asymmetric and the full band needs to be stored.

2.5 Boundary Conditions

There are two types of interface that need to be captured in the numerical simulation: the interface between air and water, i.e. the free surface; the interface between solid and liquid or water, i.e. the body boundary. They are both distinguished by a density function ϕ_m, which can be solved by the advection equation.

$$\frac{\partial \phi_m}{\partial t} + u_i \frac{\partial \phi_m}{\partial x_i} = 0 \tag{2.23}$$

where $m = 1, 2, 3$ denote liquid, solid and air phases, respectively; $\phi_1 = 1$ for liquid and zero for the air and solid; $\phi_2 = 1$ for solid and zero for the air and liquid; and $\phi_3 = 1$ for air and zero for the air and liquid.

Solving Eq. 2.23 directly will produce numerical diffusion and tend to smear the initial sharpness of the interfaces. In this work, rather than ϕ_m itself, its transformation, $F(\phi_m)$, is calculated by the CIP method. If we specify $F(\phi_m)$ as a function of ϕ_m only, the new function $F(\phi_m)$ is also governed by Eq. 2.23. Therefore,

we have

$$\frac{\partial F(\phi_m)}{\partial t} + u_i \frac{\partial F(\phi_m)}{\partial x_i} = 0 \tag{2.24}$$

In this work, a tangent function is used for the transformation (Yabe et al., 2001), i.e.,

$$F(\phi_k) = \tan[(1-\epsilon)\pi(\phi_m - 1/2)] \tag{2.25}$$

$$\phi_m = \tan^{-1} F(\phi_m)/[(1-\epsilon)\pi] + 1/2 \tag{2.26}$$

where ϵ is a small positive constant. The factor $(1-\epsilon)$ enables us to get around $-\infty$ for $\phi_m = 0$ and ∞ for $\phi_m = 1$, and to tune for desired steepness of the transition layer. The parameter ϵ needs to be chosen artificially before calculation. According to the tangent function, a smaller ϵ results in a numerically sharper slope across the transition layer.

2.5.1 Calculation Method for the Density Function for a Two-Dimensional Rigid Body

A direct Lagrangian computational method has been employed to determine the density function, ϕ_2, for the solid phase. The basic idea for this method is to map the geometry information of a moving body to a fixed Cartesian grid and to obtain the solid body boundary positions accurately without any numerical diffusion. For a two-dimensional wedge, the main scheme is as described below:

1. The coordinates for the end points of the wedge (P_1, P_2, P_3) are calculated by a Lagrangian method at each time step, as shown in Fig. 2-8.

$$x_{Pk} = x^*_{Pk} + u\Delta t$$

$$y_{Pk} = y^*_{Pk} + v\Delta t$$

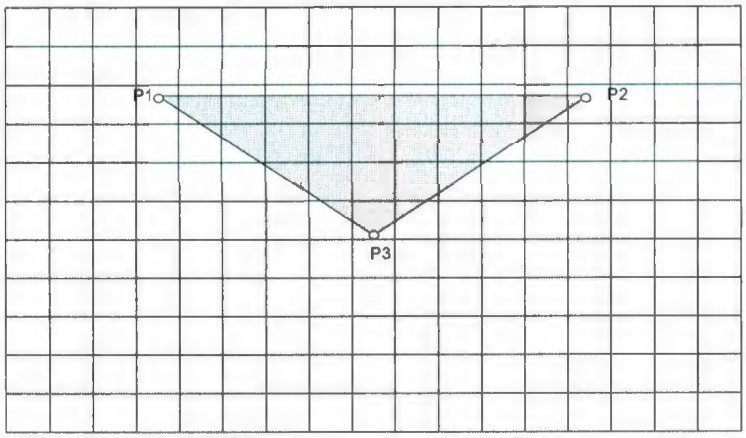

Figure 2-8: Two-dimensional wedge in a grid

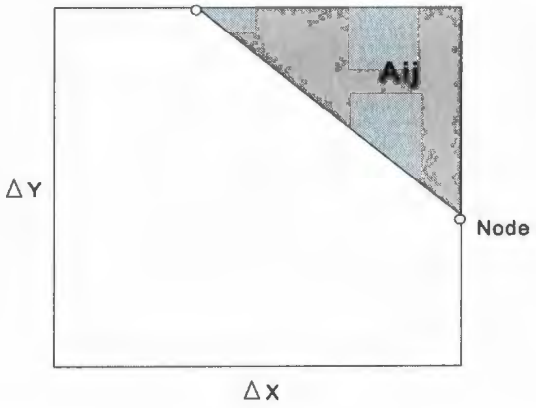

Figure 2-9: Density function for a boundary cell

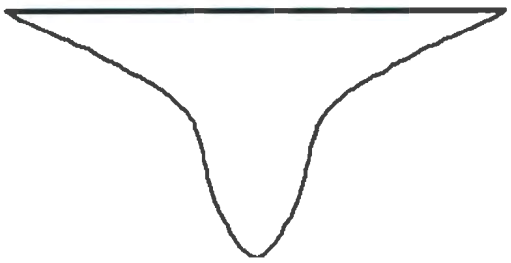

Figure 2-10: The geometry of a real ship section

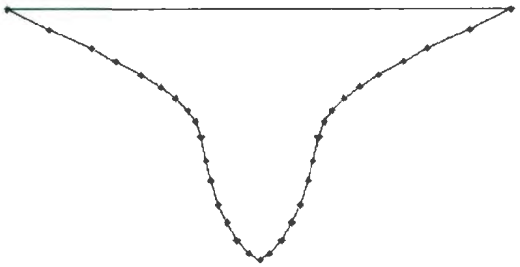

Figure 2-11: A real ship section represented by line segments

2. For each computational cell, if there are more than two nodes intersected by the body surface, the cell is considered one including the solid-body boundary, and the area of the solid body in this cell is computed to determine ϕ_2, as shown in Fig. 2-9.

$$\phi_{2ij} = A_{ij}/\Delta x_i/\Delta y_j$$

For a more complex geometry body, e.g., a real ship section (Fig. 2-10), the body boundary is approximated by a series of straight line segments, as shown in Fig. 2-11. Steps 1 and 2 are applied for each straight line. Coordinates of the nodes of line segments are calculated and the density function for each computational cell can then be determined.

2.6 Hydrodynamic Forces on the Moving Solid Body

The hydrodynamic force acting on the solid body, F_i, can be calculated by integrating the pressure and skin friction over the body surface:

$$F_i = F_i^{(P)} + F_i^{(V)} = \oint_A (-p\delta_{ik})n_k dA + \oint_A 2\mu S_{ik} n_k dA \tag{2.27}$$

where $F_i^{(P)}$ represents the force due to the pressure, and $F_i^{(V)}$ represents the force due to the friction, A denotes the surface of the solid body, and n_k is the kth component of the outward unit normal vector.

The forces can also be calculated by integration over the whole computation domain. Applying Gauss's theorem to Eq. 2.27, we obtain

$$F_i = F_i^{(P)} + F_i^{(V)} = -\oint_\Omega \frac{\partial p}{\partial x_i}\phi_2 d\Omega + \oint_\Omega \frac{\partial(2\mu s_{ik})}{\partial x_k}\varphi_2 d\Omega \tag{2.28}$$

where Ω denotes the whole computation domain and ϕ_2 is the density function of solid. Note that for the slamming problem, the skin friction is relatively small and is neglected in the computation, therefore,

$$F_i = -\oint_\Omega \frac{\partial p}{\partial x_i}\phi_2 d\Omega \tag{2.29}$$

The advantage of Eq. 2.29 is that we do not need to know the exact position and orientation of the boundary surface. Eq. 2.29 is adopted in this work.

2.7 Summary of the Computation

The computational procedure for the water entry problem is summarized in Fig. 2-12. The time integration of governing equations is based on the Euler method and

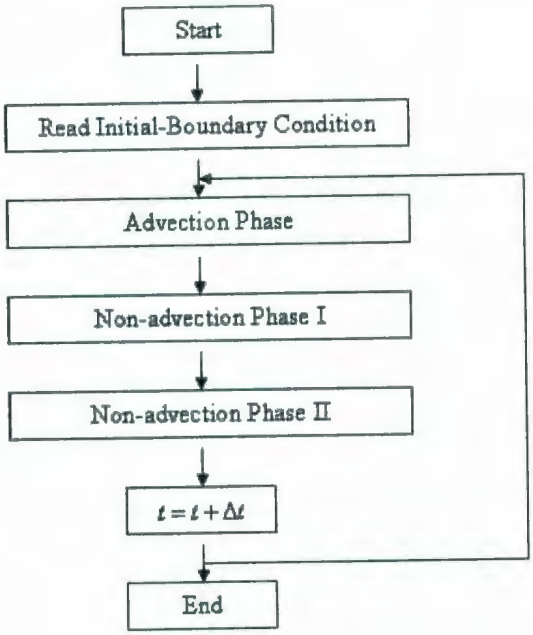

Figure 2-12: Computational procedure of two-dimensional flow

a fractional step method. For the advection equations, the finite difference method is employed. For non-advection phases, a Poisson equation for the pressure is solved by the Conjugate Gradient iterative solver. Boundary conditions including the free surface boundary and the solid boundary are determined from the density function. When the pressure distribution and velocity are obtained, the hydrodynamic force can be calculated.

Chapter 3

Numerical Results and Discussions

The symmetric and asymmetric water entry problems of two dimensional sections into calm water were solved by using the CIP-based finite difference method as discussed in previous sections. Computations were first carried out for symmetric water entry of wedges with deadrise angles of 30^o, 40^o and 60^o. The pressure distributions, free surface elevations and hydrodynamic forces are presented. The free surface elevations of a wedge with deadrise angle of 45^o during asymmetric drop (tilt angle of 20^o) were then computed. Numerical results by the CIP method are compared with experimental results and solutions by the BEM, the VOF method, and the SPH method. The water entry of a bow flare section is also presented.

In the computations, the water density and viscosity are given as ρ_{water} =

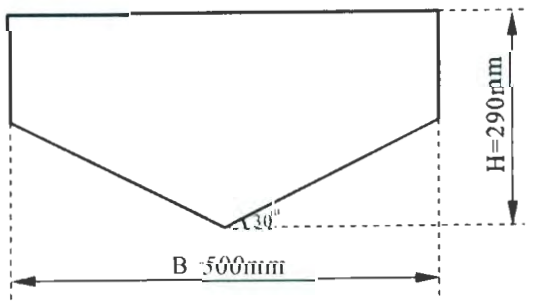

Figure 3-1: Geometry of the wedge section in the drop test

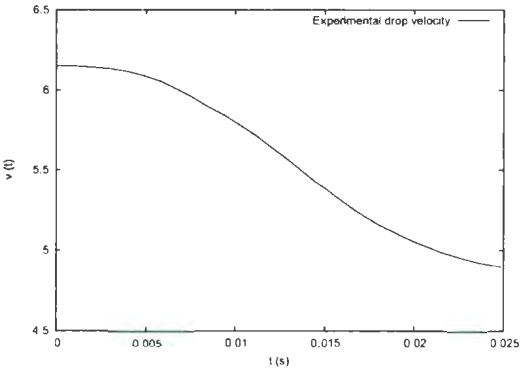

Figure 3-2: Velocities of the wedge with deadrise of 30^0 during the drop test

$1000kg/m^3$ and $\mu_{water} = 0.001kgm^{-1}s^{-1}$, respectively. Those of the air are set as $\rho_{air} = 1kg/m^3$ and $\mu_{air} = 10^{-5}kgm^{-1}s^{-1}$, respectively. Uniform grid spacing is used in the computations for water entry of wedges, and non-uniform grid is employed in the water entry of a bow flare section.

3.1 Symmetric Water Entry

Computations were first carried out for the symmetric water entry of a wedge with deadrise angle of 30^o. The geometry of the wedge is given in Fig. 3-1. Note that Zhao *et al.* (1996) conducted a drop test for such a wedge at MARINTEK and computed the pressure and the hydrodynamic force on the wedge using a boundary element method. The breadth, B, of the test section is $0.5m$ and the maximum drop height is about $2.0m$. The vertical velocities of the wedge are given in Fig. 3-2.

3.1.1 Convergence Study

To investigate the convergence of the solution to the time step and the grid spacing, the hydrodynamic forces during the water entry were computed by using various time steps and grid spacings. First, a constant time step was set as $0.0000325s$ and different grid spacings were used. The results are given in Fig. 3-3. The smallest grid spacing

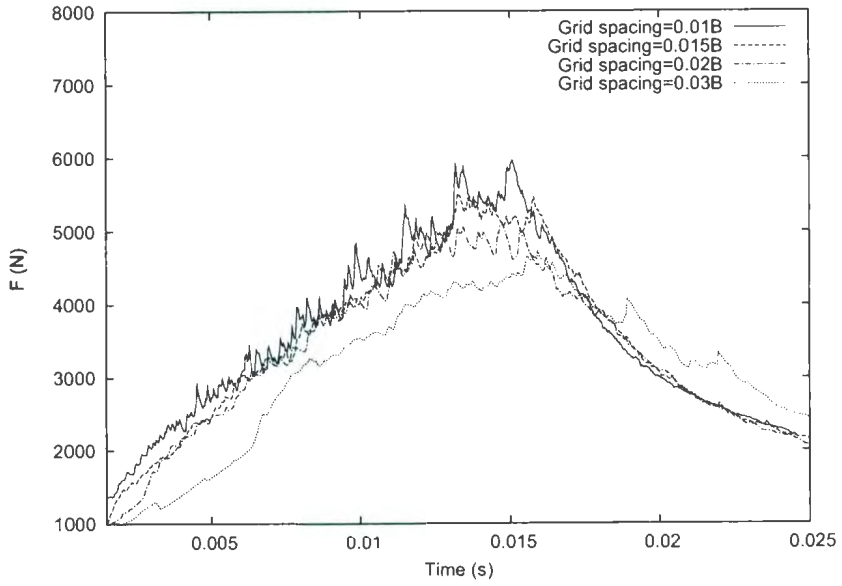

Figure 3-3: Sensitivity of hydrodynamic force to the grid spacing

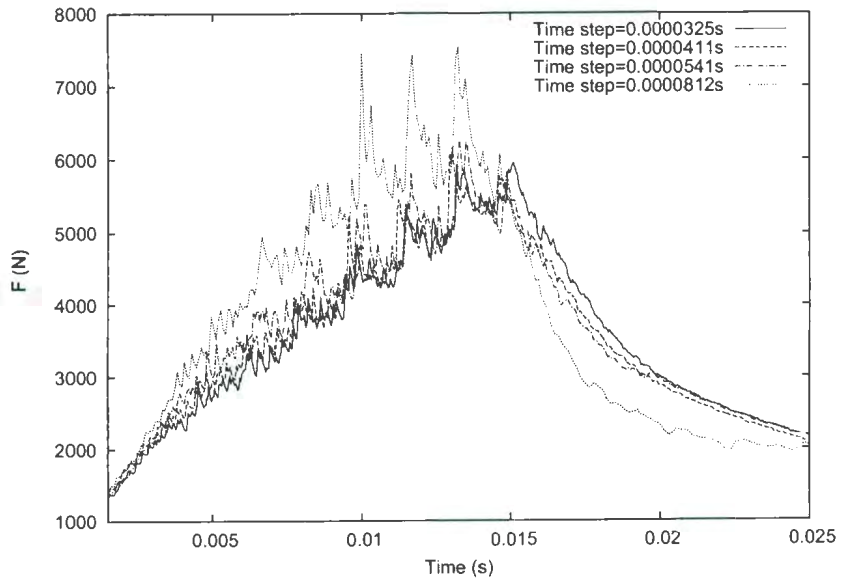

Figure 3-4: Sensitivity of hydrodynamic force to the time step

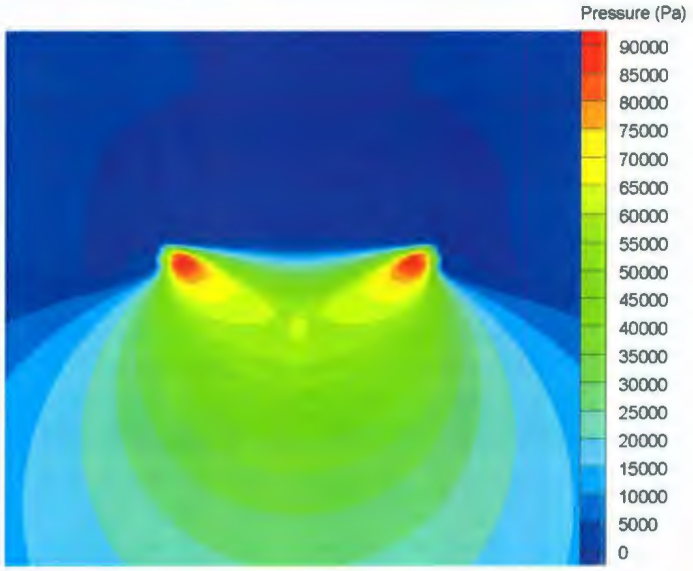

Figure 3-5: Pressure distribution on the wedge with a deadrise angle 30^o before the flow separates

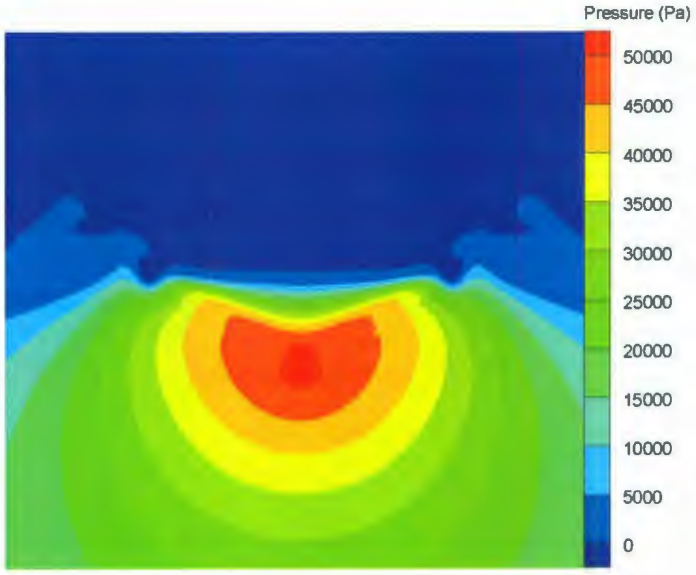

Figure 3-6: Pressure distribution on the wedge with a deadrise angle 30^o after the flow separates

is $0.01B$, and the greatest one is $0.03B$, where B is the width of the wedge. A constant grid spacing was then set as $0.01B$ and various time steps ranging from 0.0000325 seconds to 0.0000812 seconds were used. As shown in Figs. 3-3 and 3-4, the numerical solutions converge as the grid spacing and the time step decreased. In the following computations, the grid spacing and the time step were set as $0.01B$ and 0.0000325 second, respectively.

3.1.2 Pressure Distribution, Hydrodynamic Forces and Free Surface Elevation

Figure 3-5 presents the pressure distribution on the wedge surface and the computational domain at the time instant when the spray roots of the jets reach the separation points. Fig. 3-6 shows the pressure distribution in the computational domain after the flow separates. It can be shown from these figures that the maximum pressure occurs around the separation points before the flow separation occurs, and after flow separates the maximum pressure near the separation points drops fast and maximum pressure moves to the keel of the wedge.

The pressure distribution on the wedge surface was then compared with the fully nonlinear solution based on the boundary element method by Zhao *et al.* (1996) in Fig. 3-7. They in general agree well. The discrepancies at the separation points are because the separation point predicted by the CIP method and the boundary element method is slightly different.

The time series of the computed hydrodynamic forces are given in Fig. 3-8 and compared with the experimental results (Zhao *et al.*, 1996), the fully nonlinear solution by Zhao *et al.* (1996) and the numerical solution by the volume of fluid (VOF) method (Kleefsman *et al.*, 2005). In the fully nonlinear solution, the viscosity and the compressibility of water are neglected, and the Laplace equation is solved by the boundary element method. The VOF results are based on the finite volume method for solving the Navier-Stokes equation and the VOF method for capturing

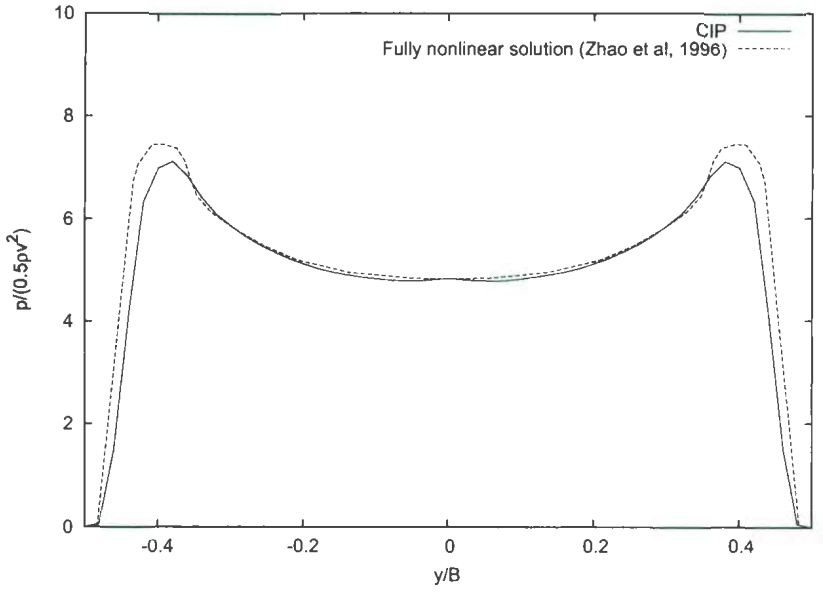

Figure 3-7: Pressure distribution on the wedge with deadrise angle 30^o when the spray roots of the jets reach the separation points

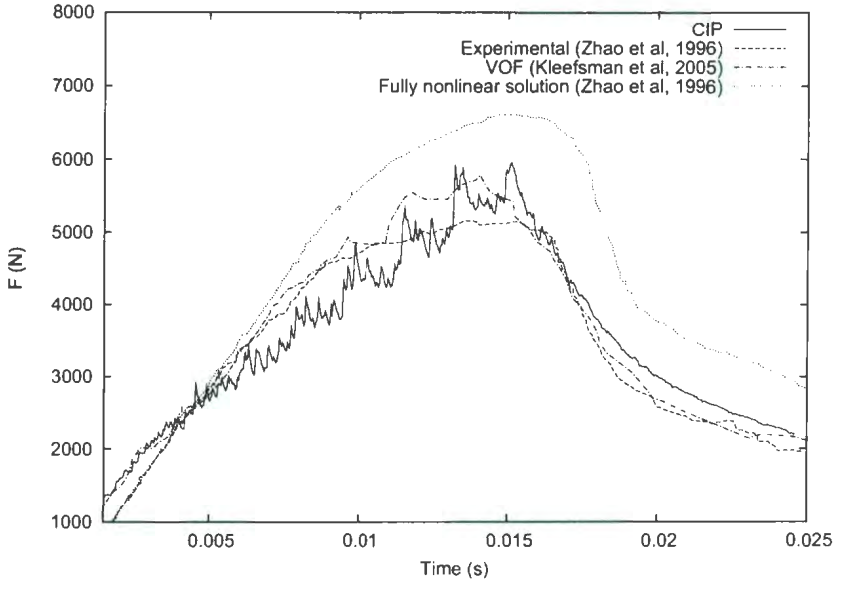

Figure 3-8: Time history of the vertical slamming force on a wedge with deadrise angle 30^o

the free surface. The numerical solution by the CIP method is in agreement with the experimental results and that by the VOF method. The fully nonlinear solution overestimates the hydrodynamic forces. Fig. 3-8 shows that the hydrodynamic force increases at the early stage of the water entry and reduces quickly after flow separation.

Figures 3-9 to 3-12 present the free surface deformation during the water entry of the wedge at several time instants. As we can see, after the wedge enters the free surface, two jets are generated on both sides of the part of the wedge in the air. At about $t = 0.015s$, the flow separation occurs, and after $t = 0.025s$, the wedge is immersed completely by the water.

3.2 Symmetric Water Entry for Wedges with Various Deadrise Angles

Pressure distributions on wedges with different deadrise angles were also computed. The deadrise angles are 30^o, 40^o and 60^o, respectively. These wedges enter the water at a constant vertical velocity. Numerical results are shown in Figs. 3-13 to 3-15. All the results are compared with numerical solutions by the boundary element method (Zhao and Faltinsen, 1993). The agreement is generally favorable.

From these figures, we can find that the sharp-peaked pressure occurs close to the jet flow area for wedges with small deadrise angles. For the wedge with deadrise angle of 60^o, the maximum pressure point tends to move to the keel of the wedge. The value of maximum pressure drops quickly for wedges with larger deadrise.

The computed free surface elevations for wedges with 30^o and 45^o deadrise angles were compared with the test results by Greenhow and Lin (1987) and the numerical solution by the VOF method (Kleefsman *et al.*, 2005) in Fig. 3-16. The visual comparison indicates that the predicted free surface elevation is in a good agreement with the VOF solution and the experimental results.

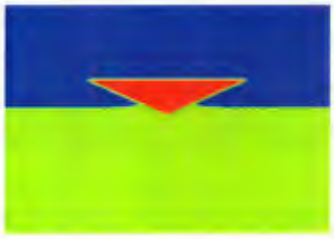

Figure 3-9: Free surface elevation during the water entry of a wedge with deadrise angle 30^o, $t = 0.005s$

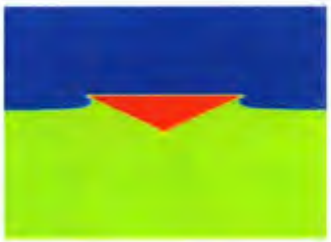

Figure 3-10: Free surface elevation during the water entry of a wedge with deadrise angle 30^o, $t = 0.015s$

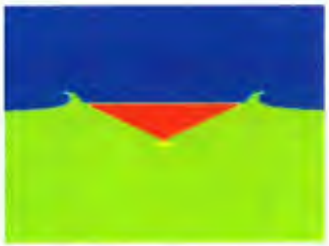

Figure 3-11: Free surface elevation during the water entry of a wedge with deadrise angle 30^o, $t = 0.02s$

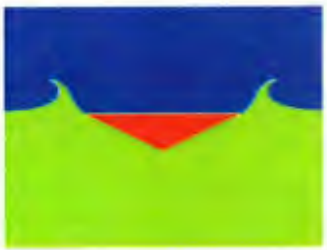

Figure 3-12: Free surface elevation during the water entry of a wedge with deadrise angle 30^o, $t = 0.025s$

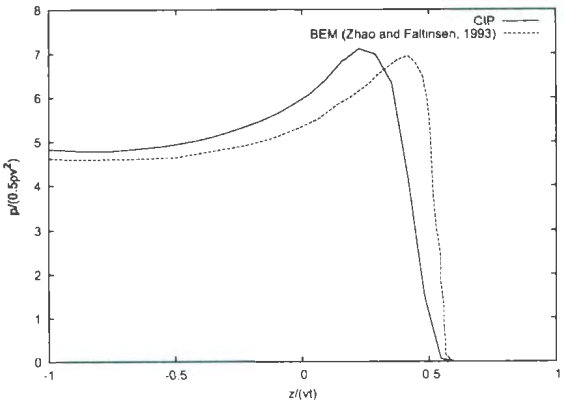

Figure 3-13: Pressure distribution around wedge with deadrise angle 30^o

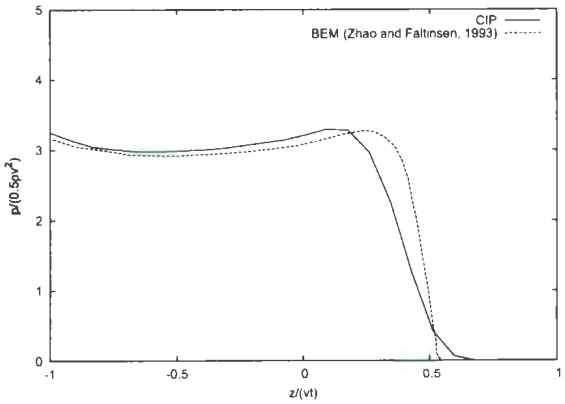

Figure 3-14: Pressure distribution around wedge with deadrise angle 40^o

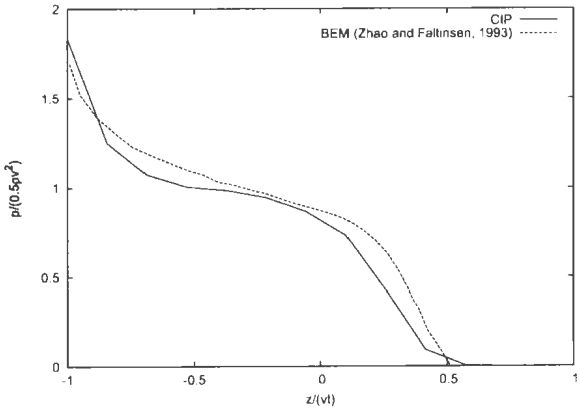

Figure 3-15: Pressure distribution around wedge with deadrise angle 60^o

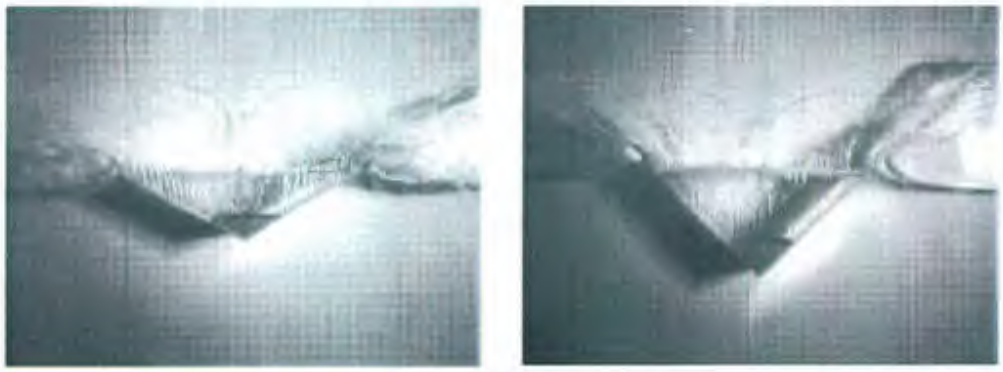

(a) Experimental (Greenhow and Lin, 1983)

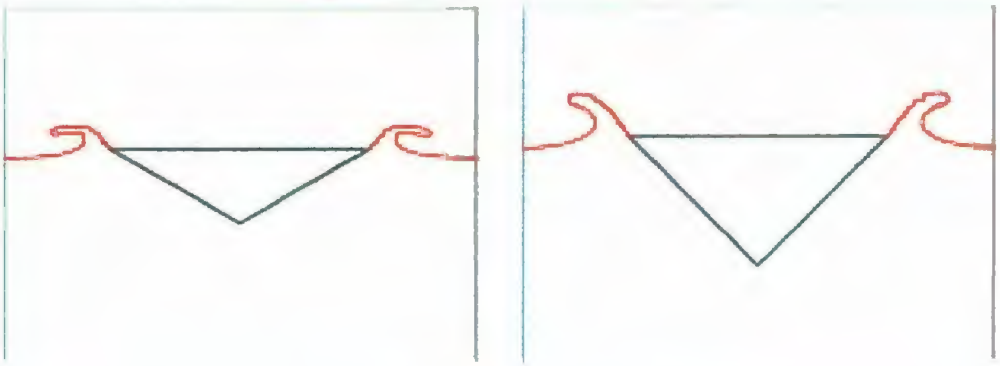

(b) VOF (Kleefsman *et al.*, 2005)

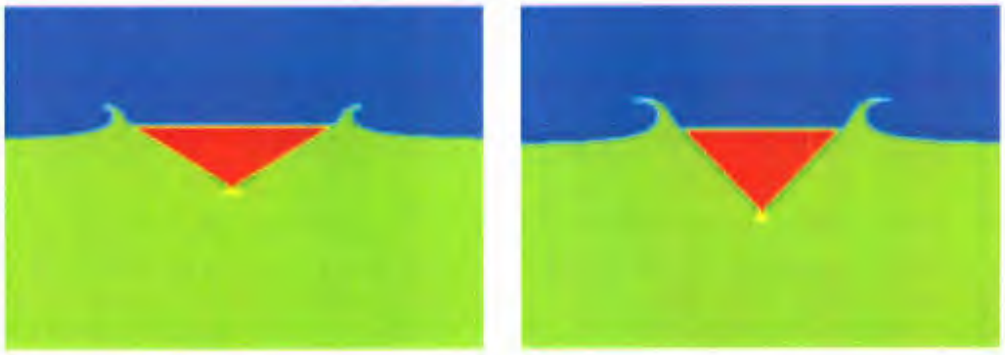

(c) CIP

Figure 3-16: Snapshots of wedge entry with deadrises angle 30^o (left) and 45^o (right)

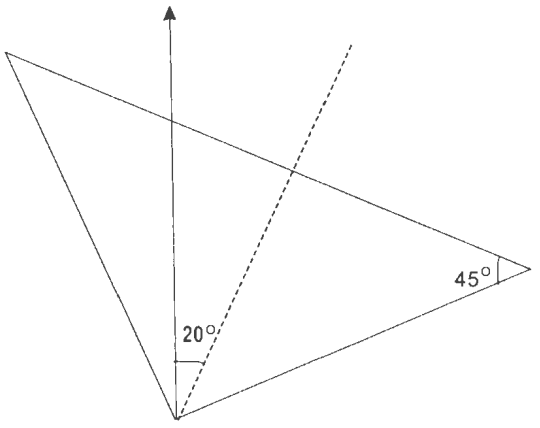

Figure 3-17: Geometry of the wedge section in the drop test

3.3 Asymmetric Water Entry

The computation was extended to a wedge entering the calm water with a tilt angle. This is the case of asymmetric water-entry of a wedge. In the real situation of ship slamming, the ship does not always experience symmetric water entry due to roll motion and asymmetric waves with respect to ship. Such an asymmetric water-entry can induce hydrodynamic impact which is significantly different from symmetric cases. A drop test was carried out by Kim *et al.* (2007) to observe the physical phenomena of two-dimensional asymmetric water-entry of a wedge. The wedge is $0.2m$ wide with a 45^o deadrise angle and the tilt angle is 20^o, as shown in Fig. 3-17. The drop velocity was $2.42m/s$.

Numerical results of the free surface elevation by the CIP method are compared with the experimental data in Fig. 3-18. Comparison was also made with the numerical solution using the SPH method by Kim *et al.* (2007). In the SPH method, a finite number of particles which have physical properties including mass, density and pressure, are distributed in the fluid domain. The movement of these particles can be obtained by solving the Euler equation and the continuity equation. The agreement between the CIP and the SPH methods is satisfactory. From these figures, we find that the jets on the two sides of wedge are different due to the tilt angle.

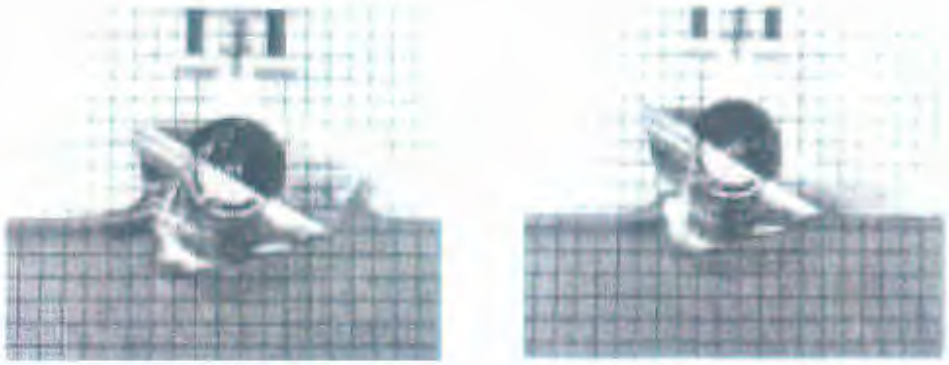

(a) Experiment (Kim *et al.*, 2007)

(b) SPH (Kim *et al.*, 2007)

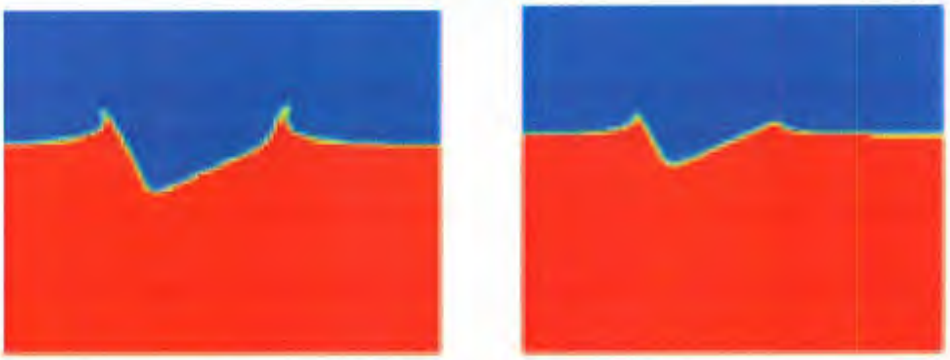

(c) CIP

Figure 3-18: Free surface evolution during asymmetric drop: deadrise angle 45°; tilt 20°; velocity $2.42 m/sec$

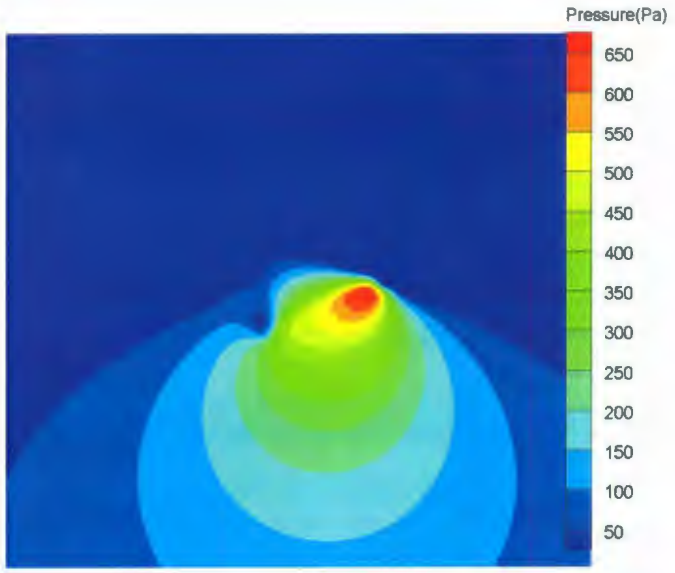

Figure 3-19: Pressure distribution on the wedge with a tilt angle 20^o before the flow separates

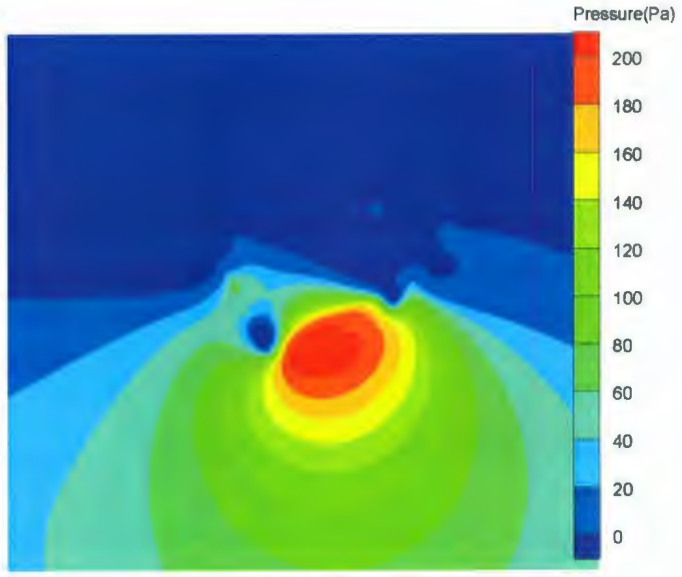

Figure 3-20: Pressure distribution on the wedge with a tilt angle 20^o after the flow separates

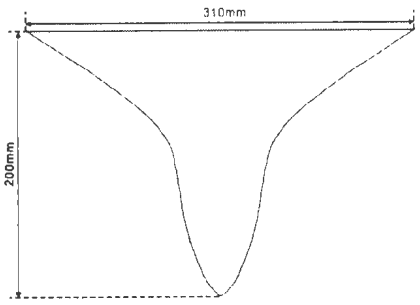

Figure 3-21: The geometry of a bow flare section

Figures 3-19 and 3-20 show the pressure distribution on the wedge surface and the computational domain for the asymmetric water-entry case. The higher pressure occurs on the side of the wedge with smaller deadrise angle. Fig. 3-19 presents the pressure contours before the flow separation, and the maximum pressure is observed on the separation point of the side with smaller deadrise angle. As shown in Fig. 3-20, after the flow separation, the maximum pressure moves to the keel of the wedge and value of the maximum pressure drops quickly,

3.4 Water Entry of a Bow Flare Section

The numerical scheme based on the non-uniform discretization scheme has the potential to decrease the computing time while maintaining the accuracy of solutions.

The computation program was extended to compute the water entry of a bow flare section based on the non-uniform grid. A drop test for the bow flare section was carried out by Zhao *et al.* (1996) at MARINTEK. The geometry of the bow flare was given in Fig. 3-21. Fig. 3-22 presents the vertical velocity in the drop test, which is also used in the numerical simulation.

The numerical grid, as illustrated in Fig. 3-23, varys in the computational domain. Uniform grids with smallest spacings are used around the bow flare section. The smallest non-dimensional lengths are $\triangle x/B = 0.01$ and $\triangle y/B = 0.01$. Non-uniform

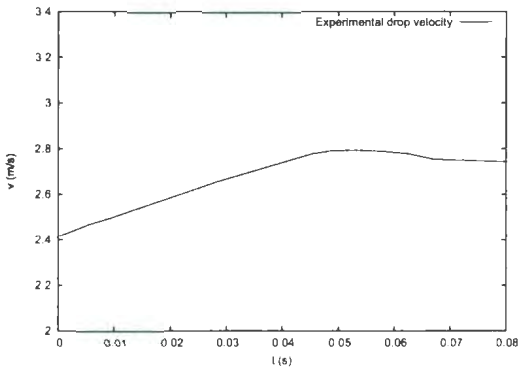

Figure 3-22: Velocity of the bow flare section during the drop test

grids which follow cosine function distribution are used elsewhere.

The time series of the computed hydrodynamic forces are given in Fig. 3-24 and compared with the experimental results (Zhao *et al.*, 1996). There is a good agreement between numerical and experimental results in the earlier time instants. The discrepancy is larger at a later stage. Further investigation is needed.

Figure 3-25 shows the pressure distribution around the bow flare when the flow separates. Similar to the water entry of wedges, the maximum pressure occurs near the separation points.

The free surface elevations were also computed by the CIP method. Fig. 3-26 presents the free surface elevation when the flow separation occurs. As we can see, two jets are generated and the breaking wave occurs.

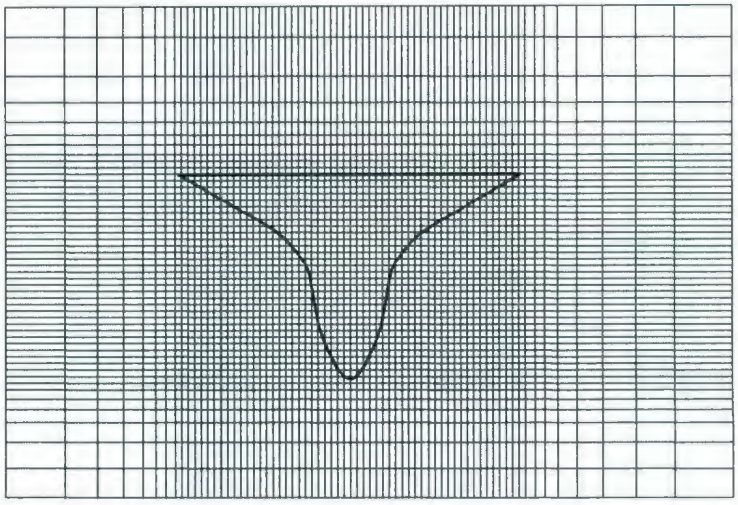

Figure 3-23: Grid distribution of the bow flare section

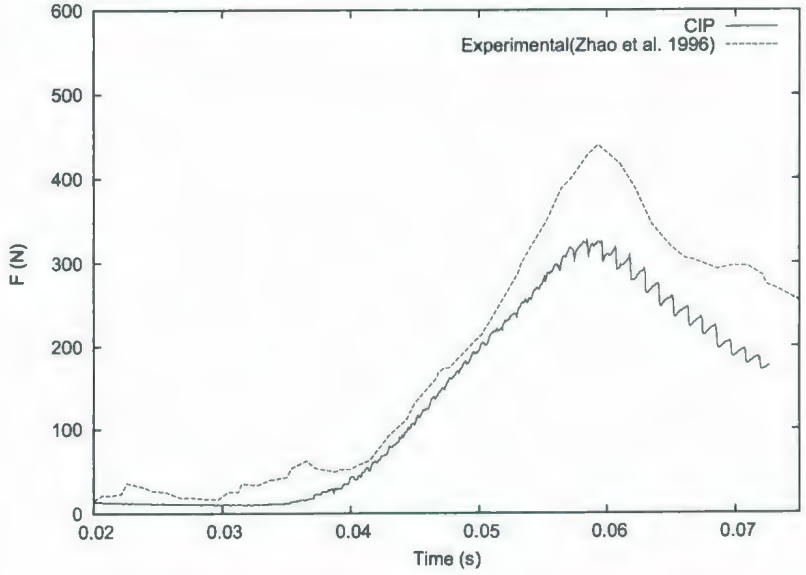

Figure 3-24: Hydrodynamic force on a bow flare section

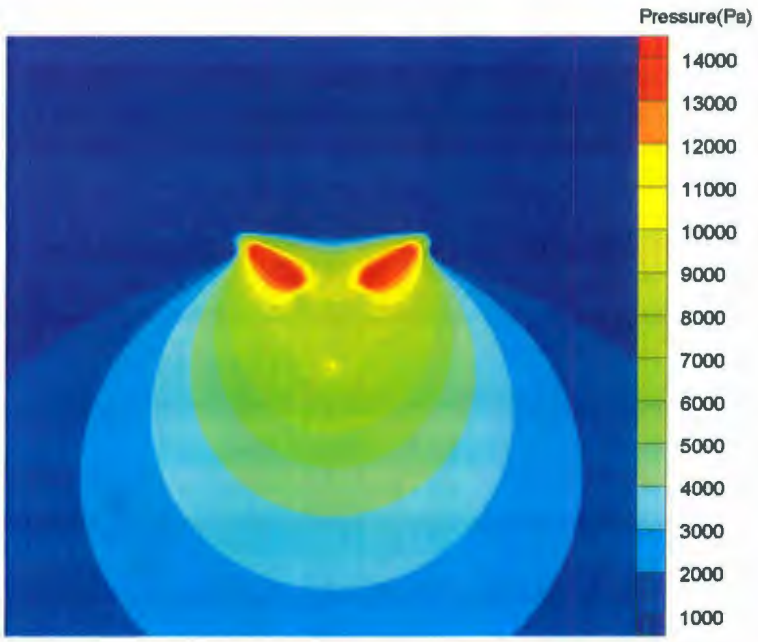

Figure 3-25: Pressure distribution around the bow flare when the flow separates

Figure 3-26: Free surface elevation when the flow separates

Chapter 4

Conclusions

The nonlinear water entry problem governed by the Navier-Stokes equations was solved by a CIP based finite difference method on a fixed Cartesian grid. In the computation, the CIP method was employed for the advection calculations and a pressure-based algorithm was applied for the non-advection calculations. The free surface and the body boundaries were captured using density functions. For the pressure calculation, a Poisson-type equation was solved at each time step by the Conjugate Gradient iteration method.

Validation studies have been carried out for symmetric and asymmetric water entry of wedges with different deadrise angles and a bow flare section. Pressures, free surface elevations and hydrodynamic forces were computed and compared with experimental results and numerical solutions by the boundary element method, the VOF method and the SPH method. The solutions by the CIP method are in a good agreement with others. It has been demonstrated that the CIP method is able to capture the highly distorted free surface elevation and to accurately predict pressures and hydrodynamic forces on wedges entering the calm water.

For future work, studies will be carried out to extend the CIP method to solve the three-dimensional water entry problem of bodies of arbitrary geometry.

References

Armand, J.L. and Cointe, R., 1986, Hydrodynamic impact analysis of a cylinder, Proceedings of the Fifth International Offshore Mechanics and Arctic Engineering, Tokyo, Japan, Vol. 1, pp. 609-634.

Chuang, J.M., Zhu, W. and Qiu, W., 2006, Numerical solutions of 2-D water entry problem, Proceedings of ISOPE2006, San Francisco.

Cointe, R., 1991, Free surface flows close to a surface-piercing body, Mathematical Approaches in Hydrodynamics (ed. T. Miloh), Soc. Ind. Appl. Maths, Philadelphia, pp. 319-334.

Dobrovol'skaya, Z.N., 1969, On some problems of similarity flow of fluid with a free surface, Journal of Fluid Mechanics, Vol. 36, pp. 805-829.

Greenhow, M., 1987, Wedge entry into initially calm water, Applied Ocean Research, Vol. 9, pp. 214-223.

Greenhow, M. and Lin, W.M., 1983, Nonlinear free surface effects: experiments and theory, Report No. 83-19, Department of Ocean Engineering, MIT, Cambridge, MA.

Howison, S.D., Ockendon, J.R. and Wilson, S.K., 1991, Incompressible water-entry problems at small deadrise angles, Journal of Fluid Mechanics, Vol. 222, pp. 215-230.

Hu, C. and Kashiwagi, M., 2004, A CIP-based method for numerical simulations of violent free-surface flow, J. Mar. Sci. Technol., Vol. 9, pp.143-157.

Hu, C., and Kashiwagi, M., 2007, Numerical and experimental studies on three-dimensional water on deck with a modified Wigley model, Proceedings of 9th International Conference on Numerical Ship Hydrodynamics, Ann Arbor, Michigan.

Judge, J., Troesch, A., and Perlin, M., 2004, Initial water impact of a wedge at vertical and oblique angles, Journal of Engineering Mathematics, Vol. 48. pp. 279-303.

Kim, Y.W., Kim, Y., Liu, Y.M., and Yue, D., 2007, On the water-entry impact problem of asymmetric bodies, Proceedings of 9th International Conference on Numerical Ship Hydrodynamics, Ann Arbor, Michigan.

Kleefsman, K.M.T., Fekken, G., Veldman, A.E.P., Iwanowski, B. and Buchner, B., 2005, A volume-of-fluid based simulation method for wave impact problems, Journal of Computation Physical, Vol. 206, pp. 363-393.

Kishev, Z. R., Hu, C., and Kashiwagi, M., 2006, Numerical simulation of violent sloshing by a CIP-based method, J. Mar. Sci. Technol., Vol. 11, pp. 111-122.

Lafrati, A. and Carcaterra, A., 2000, Hydroelastic analysis of a simple oscillator impacting the free surface, Journal of Ship Research, Vol. 44, No. 4, pp. 278-289.

Lin, W.M., Newman, J.N. and Yue, D.K., 1984, Nonlinear forced motions of floating bodies, Proceedings of the 15th Symposium on Naval Hydrodynamics, Hamburg, pp. 33-47.

Nonaka, N. and Nakayama, T., 1996, A unified method for the numerical analysis of compressible and incompressible viscous flows, Computational Mechanics, Vol. 18, pp. 369-376.

Vinje, T. and Brevig, P., 1981, Nonlinear ship motions, Proceedings of the 3rd International Conference on Numerical Ship Hydrodynamic, Paris, pp. 257-266.

Wagner, H., 1932, *Über* stoss-und Gleitvergängean der Oberfläche von Flüssigkeiten, Z. Angew, Math Mech, Vol. 12, No. 4, pp. 192-235.

Xiao, F., 1999, A computational model for suspended large rigid bodies in 3D

unsteady viscous flows, Journal of Computational Physics, Vol. 155, pp. 348-379.

Yabe, T., Xiao, F. and Utsumi, T., 2001, The constrained interpolation profile method for multiphase analysis, Journal of Computational Physics, Vol. 169, pp. 556-593.

Yabe, T., 1991, A universal cubic interpolation solver for compressible and incompressible fluids, Shock Waves, Vol. 1, pp. 187-195.

Yabe, T., Takizawa, K., Chino, M., Imai, M. and Chu, C.C., 2005, Challenge of CIP as a universal solver for solid, liquid and gas, International Journal for Numerical Methods in Fluids, Vol. 47, pp. 655-676.

Zhao, R. and Faltinsen, O., 1993, Water entry of two-dimensional bodies, J. Fluid Mech., Vol. 246, pp. 593-612.

Zhao, R., Faltinsen, O. and Aarsnes, J., 1996, Water entry of arbitrary two-dimensional sections with and without flow separation, Proceedings of 21st Symposium on Naval Hydrodynamics, Trondheim, Norway.

Zhu, X., Faltinsen, O. M. and Hu, C., 2005, Water entry and exit of a horizontal circular cylinder, 24th International Conference on Offshore Mechanics and Arctic Engineering, Halkidiki, Greece.